Received: 7 February 2023 | Revised: 14 June 2023 | Accepted: 3 July 2023

DOI: 10.1002/hbm.26421

RESEARCH ARTICLE

WILEY

Data-driven electrical conductivity brain imaging using 3 T MRI

Kyu-Jin Jung[1] | Stefano Mandija[2,3] | Chuanjiang Cui[1] | Jun-Hyeong Kim[1] | Mohammed A. Al-masni[4] | Thierry G. Meerbothe[2,3] | Mina Park[5] | Cornelis A. T. van den Berg[2,3] | Dong-Hyun Kim[1]

[1]Department of Electrical and Electronic Engineering, Yonsei University, Seoul, Republic of Korea

[2]Computational Imaging Group for MR Therapy and Diagnostics, University Medical Center Utrecht, Utrecht, The Netherlands

[3]Department of Radiotherapy, University Medical Center Utrecht, Utrecht, The Netherlands

[4]Department of Artificial Intelligence, College of Software & Convergence Technology, Daeyang AI Center, Sejong University, Seoul, Republic of Korea

[5]Department of Radiology, Gangnam Severance Hospital, Yonsei University College of Medicine, Seoul, Republic of Korea

Correspondence
Dong-Hyun Kim, Department of Electrical and Electronic Engineering, Yonsei University, Seoul, Republic of Korea.
Email: donghyunkim@yonsei.ac.kr

Funding information
Institute for Information & Communications Technology Planning & Evaluation (IITP), Grant/Award Number: IITP-2022-2020-0-01461; National Research Foundation of Korea (NRF), Grant/Award Number: NRF-2022R1A4A1030579; Netherlands Organisation for Scientific Research (NWO), Grant/Award Number: 18078

Abstract

Magnetic resonance electrical properties tomography (MR-EPT) is a non-invasive measurement technique that derives the electrical properties (EPs, e.g., conductivity or permittivity) of tissues in the radiofrequency range (64 MHz for 1.5 T and 128 MHz for 3 T MR systems). Clinical studies have shown the potential of tissue conductivity as a biomarker. To date, model-based conductivity reconstructions rely on numerical assumptions and approximations, leading to inaccuracies in the reconstructed maps. To address such limitations, we propose an artificial neural network (ANN)-based non-linear conductivity estimator trained on simulated data for conductivity brain imaging. Network training was performed on 201 synthesized T2-weighted spin-echo (SE) data obtained from the finite-difference time-domain (FDTD) electromagnetic (EM) simulation. The dataset was composed of an approximated T2-w SE magnitude and transceive phase information. The proposed method was tested three in-silico and in-vivo on two volunteers and three patients' data. For comparison purposes, various conventional phase-based EPT reconstruction methods were used that ignore B_1^+ magnitude information, such as Savitzky–Golay kernel combined with Gaussian filter (S-G Kernel), phase-based convection-reaction EPT (cr-EPT), magnitude-weighted polynomial-fitting phase-based EPT (Poly-Fit), and integral-based phase-based EPT (Integral-based). From the in-silico experiments, quantitative analysis showed that the proposed method provides more accurate and improved quality (e.g., high structural preservation) conductivity maps compared to conventional reconstruction methods. Representatively, in the healthy brain in-silico phantom experiment, the proposed method yielded mean conductivity values of 1.97 ± 0.20 S/m for CSF, 0.33 ± 0.04 S/m for WM, and 0.52 ± 0.08 S/m for GM, which were closer to the ground-truth conductivity (2.00, 0.30, 0.50 S/m) than the integral-

based method (2.56 ± 2.31, 0.39 ± 0.12, 0.68 ± 0.33 S/m). In-vivo ANN-based conductivity reconstructions were also of improved quality compared to conventional reconstructions and demonstrated network generalizability and robustness to in-vivo data and pathologies. The reported in-vivo brain conductivity values were in agreement with literatures. In addition, the proposed method was observed for various SNR levels (SNR levels = 10, 20, 40, and 58) and repeatability conditions (the eight acquisitions with the number of signal averages = 1). The preliminary investigations on brain tumor patient datasets suggest that the network trained on simulated dataset can generalize to unforeseen in-vivo pathologies, thus demonstrating its potential for clinical applications.

KEYWORDS

Conductivity brain imaging, Electrical properties tomography, MR image synthetization, Nonlinear conductivity estimator, Phase-based EPT reconstruction

1 | INTRODUCTION

Magnetic resonance electrical properties tomography (MR-EPT) is a non-invasive measurement technique that derives electrical properties (EPs: conductivity σ and permittivity ε) of human tissues from the distribution of transmit and receive radiofrequency (RF) fields of an MR system (Haacke et al., 1991; Katscher et al., 2009). The tissue EPs distribution is not only important for estimation of the specific absorption rate (Balidemaj et al., 2017; Katscher et al., 2009; Voigt et al., 2012; Zhang et al., 2013), but clinical studies have shown its potential as a biomarker in oncology (Balidemaj et al., 2015a, 2016; Kim et al., 2016; Lazebnik et al., 2007; Lee et al., 2022; Mori et al., 2019; Shin et al., 2015; Suh et al., 2021; Tha et al., 2014, 2018).

To observe the tissue EPs, various MR-EPT reconstruction algorithms have been proposed by the arrangement of the Maxwell equations (Balidemaj et al., 2015b; Hafalir et al., 2014; Katscher et al., 2009; Liu et al., 2015; Lee et al., 2015a, 2015b; Serrallés et al., 2019; Voigt et al., 2011). Especially, in most MR-EPT algorithms, assumptions are applied to derive simplified formulas. Representatively, the piece-wise constant assumption (i.e., a homogeneous medium: $\nabla\kappa = 0$) of EP values allows the Helmholtz-based EPT reconstruction (H-EPT). However, H-EPT method produced boundary artifacts at tissue boundaries where spatial homogeneity is disrupted (van Lier et al., 2012; Voigt et al., 2011). In addition, the straight-forward computation of the Laplacian operator results in noise amplification for the noisy B_1^+ field. To address the problem, the Helmholtz equation can be reorganized by incorporating a convection-reaction term, resulting in the convection-reaction EPT (cr-EPT) (Gurler & Ider, 2017; Hafalir et al., 2014). Although the computation process for the cr-EPT is not restricted to homogeneous tissue regions, since spatial derivatives computation for noisy B_1^+ fields is still required, error and artifacts may be observed in the reconstruction results, especially in a low convective field. Integral-based methods showed robust reconstruction results for the noise amplification and boundary artifact, but the computational load may be expensive based on the iterative optimization with the regularizations (Balidemaj et al., 2015b; Guo et al., 2017; Hong et al., 2017; Schmidt & Webb, 2016; Serrallés et al., 2019).

On the other hand, some EPT reconstruction algorithms enable conductivity reconstructions using only B_1^+ phase information while ignoring B_1^+ magnitude information under certain assumptions (e.g., H-EPT: $\nabla^2\varphi^+ \gg 2\left(\nabla|B_1^+|\cdot\nabla\varphi^+\right)/\left(|B_1^+|\right)$ or cr-EPT: $\nabla|B_1^+| = 0$ and $\nabla B_z = 0$) for 1.5–3 T MR systems, so-called Phase-based EPT (Gurler & Ider, 2017; van Lier et al., 2012; Voigt et al., 2011). In addition, the transceive phase assumption, which assumes that the B_1^+ phase (φ^+) and B_1^- phase (φ^-) exhibit similarity, facilitates further adoption of the phase-based EPT approaches. Here, the B_1^+ phase can be approximated by taking half of the transceive phase information from spin-echo (SE) or balanced steady-state free precession (bSSFP) sequences, which are commonly employed in clinical routines (i.e., $\varphi^+ \approx \varphi^{\pm}/2 = (\varphi^+ + \varphi^-)/2$). Thus, the phase-based EPT approaches may hold promise for fostering further investigations and applications in the diagnosis and treatment of pathologies in clinical settings without additional MRI scans (Kim et al., 2016; Suh et al., 2021).

Despite these potential applications, phase-based EPT reconstructions still encounter challenges that lead to erroneous observations deviating from ground-truth conductivity (GTC) values, which are directly associated with underlying the assumptions (Duan et al., 2016; Lee et al., 2015b; Mandija et al., 2018; Seo et al., 2011). Some of its limitations are as follows. Firstly, phase-based EPT reconstruction algorithms ignore the B_1^+ magnitude information, leading to an overestimation in the reconstructed results (Voigt et al., 2011). Secondly, the piece-wise constant assumption of EP values allows the derivation of the simplified Helmholtz equation; however, ignoring spatial changes in the EPs leads to erroneous reconstructions, especially at tissue boundaries where spatial homogeneity is disrupted (van Lier et al., 2012; Voigt et al., 2011). Furthermore, the computation of numerical derivatives using kernel-based or fitting-based methods leads to substantial errors at the boundaries (Lee et al., 2015b;

Mandija et al., 2018; Seo et al., 2011). To address this problem, possible strategies include integrating compensating factors, such as a convection-reaction term, which allows for deviation from the piecewise constant assumption (Gurler & Ider, 2017), or employing available MR contrast information to confine derivative computations to voxels with similar intensity values (Karsa & Shmueli, 2021; Katscher et al., 2016; Lee et al., 2016). Yet, estimation errors in homogeneous regions can still be observed. Lastly, the computation of differentiation kernels causes noise amplification in the reconstructed conductivity maps (Karsa et al., 2021; Mandija et al., 2018). Thus, in situations where high signal-to-noise-ratio (SNR) levels cannot be ensured, employing image filters may be a feasible option to achieve denoising effects. However, this approach could have trade-offs, such as reduced effective resolutions or broadened boundary artifacts (Lee et al., 2015b; Shin et al., 2019; Voigt et al., 2011).

Recently, deep learning (DL) approaches have been introduced as an alternative to address the problems of the conventional MR-EPT algorithms (Gavazzi et al., 2020; Hampe et al., 2020; Inda et al., 2022; Jung, Mandija et al., 2021; Lee et al., 2021; Leijsen et al., 2022; Mandija et al., 2019). As a first attempt, the generative adversarial network (GAN) based method was proposed (Mandija et al., 2019) for estimating conductivity and permittivity using simulated B_1^+ magnitude and B_1 phase information. This study showed its feasibility to be applied to in-vivo data of a healthy volunteer. This work also investigated the significance of feeding MR contrast information to the network for better resolving tissue boundaries. Afterwards, 3D patch-based DL approach (Hampe et al., 2020) was proposed as an alternative to the phase-based EPT reconstruction algorithms using only B_1 phase information. Despite the promising results shown on patient data, the 3D patch-based DL approach, which relies only on phase information for computations, resulted in loss of detailed information due to the vulnerability of the network to noise, and limited training dataset may lead to low generalization performance.

As mentioned, conductivity maps can be retrieved by solving the Helmholtz equation, which is a non-linear partial differential equation. Recently, DL approaches have been investigated to replace the computations of non-linear partial derivative equations (Baymani et al., 2015; Ben-Shabat & Gould, 2020; Chakraverty & Mall, 2020; Jung, Lee et al., 2021; Kwon et al., 2017; Murphy et al., 2018; Raissi et al., 2019). Such artificial neural network (ANN) approaches have demonstrated that usage of DL can be advantageous in obeying spatial robustness, invariance, and conservation characteristics. This is due to the training dataset which can address the non-linear problems within model boundaries. In addition, DL-based methods have shown to be more robust under noisy observations (Ben-Shabat & Gould, 2020; Jung, Lee et al., 2021; Kwon et al., 2017; Murphy et al., 2018). Therefore, DL-based approach with physics-coupled datasets has the potential to be an alternative non-linear numerical solver for the Helmholtz equation.

This work proposes a data-driven two-dimensional (2D) patch-based non-linear conductivity estimator using ANN trained on a simulation dataset. The main contributions of this work are as follows: (1) We propose an ANN-based method for reconstructing the conductivity maps in a pixel-wise manner by incorporating the local information of images through patches (i.e., the network estimates the conductivity value for the central voxel of the input patch). The simulation training dataset was constructed based on the reported conductivity values in the literatures: cerebrospinal fluid (1.80–2.20 S/m), white matter (0.30–0.45 S/m), gray matter (0.50–0.65 S/m), and additional cylindrical structures (0.60–1.60 S/m) (Gabriel, Gabriel, & Corthout, 1996; Gabriel, Lau, & Gabriel, 1996a, 1996b; Hampe et al., 2020; Hancu et al., 2019; Liao et al., 2019; Mandija et al., 2021; Tha et al., 2014, 2018). (2) The proposed network is targeted for application to high resolution brain images (i.e., 1×1 mm^2), much higher than previous DL approaches. (3) We also incorporate the MR contrast information alongside the transceive phase data to enable the network to represent realistic characteristics of actual data. (4) The code supporting the findings of this study is openly available at https://github.com/Yonsei-MILab/Non-linear-Conductivity-Estimator.

2 | METHODS

The overall schematic diagram of the proposed work is illustrated in Figure 1. Network training was performed on synthesized dataset (T2-weighted [T2-w] SE). Details about the T2-w MR image synthetization for the training dataset are provided in Section 2.1. The data preparation and the network training process are summarized in Sections 2.2 and 2.3. In-silico testing is described in Section 2.4. Additionally, we investigated the generalizability of the network to in-vivo data in Section 2.5.

2.1 | EM simulations with T2-w MR image synthesization

The finite-difference time-domain (FDTD) electromagnetic (EM) simulation program Sim4Life (Zurich Med Tech, Zurich, Switzerland) was used to generate all the in-silico data using a birdcage coil operating in quadrature (QA) and anti-quadrature (AQ) modes at 128 MHz and two head models: Duke and Ella (human model software of IT'IS [Information Technologies in Society] Foundation) (Christ et al., 2009; Gosselin et al., 2014). The B_1^+ field ($|B_1^+|$ and φ^+) was computed in the QA mode, while the B_1^- field ($|B_1^-|$ and φ^-) was computed in the AQ mode. The transceive phase ($\varphi^{\pm}$) was determined by the sum of the simulated φ^+ and φ^-.

The geometry of the coil was set as follows: high-pass birdcage coil with 16-rungs, length = 58 cm, and diameter = 70.4 cm; RF shield: length = 68 cm, and diameter = 80.4 cm. Discretized voxel size for FDTD simulation was $x = 2$, $y = 2$, and $z = 2$ mm. With this setup, B_1^+ and B_1^- fields were calculated in QA and AQ modes from which SE images were computed as indicated in Figure 1. To increase the variability in the simulated dataset, two strategies were adopted: first, different rotations of the human models inside the coil (rotation directions: x–y plane = −10° to 10°, x–z plane = −10° to 10°) were performed; second, based on the reported conductivity values

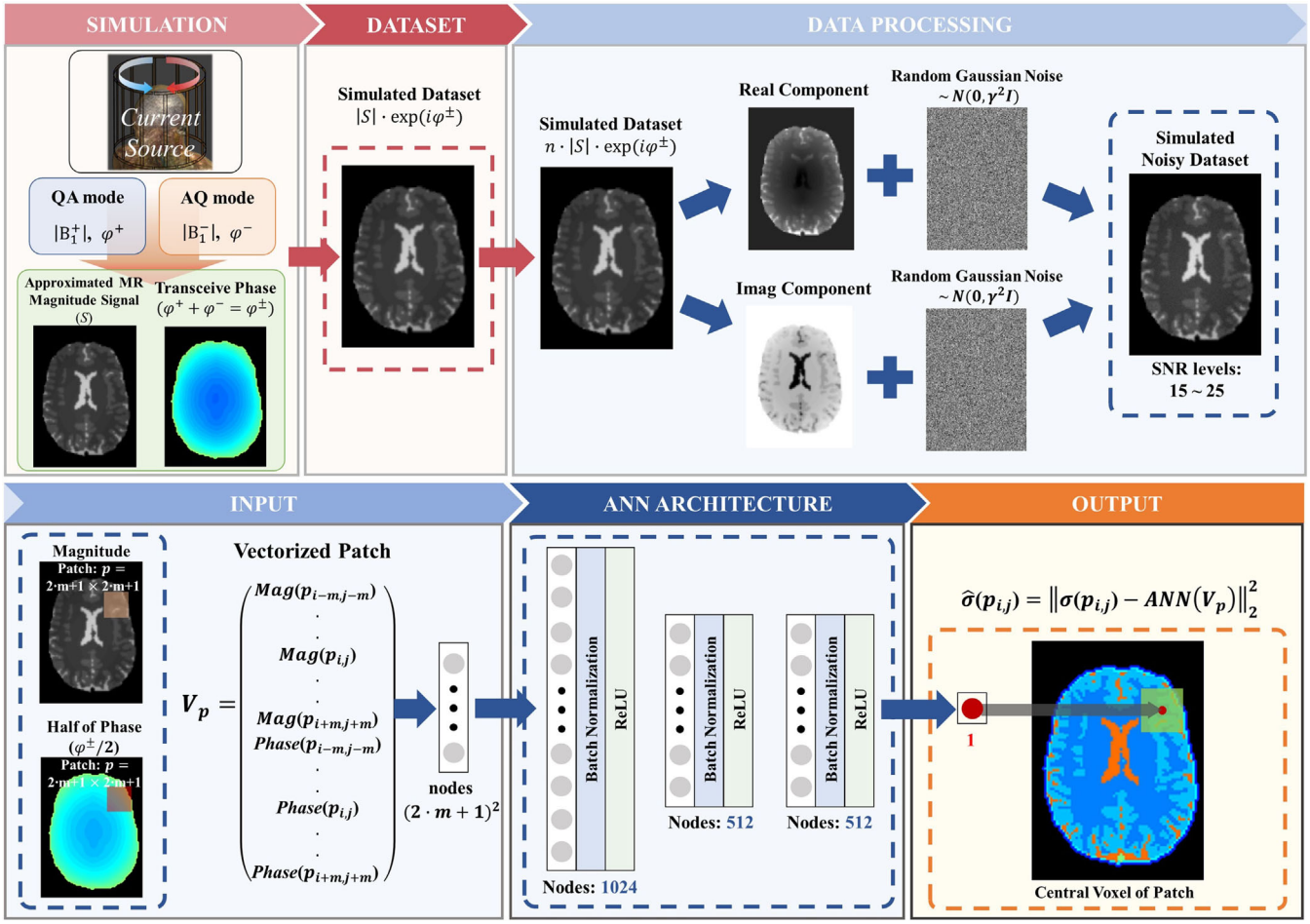

FIGURE 1 Schematic diagram of the proposed method including network training procedure. The red-series panels correspond to the training dataset generation steps. The blue-series panels summarize the network composition and all procedures that are repeated for each epoch during the network training. For the given input patch, the orange panel describes the label/output for network input. The network estimates the conductivity from the central voxel.

(Gabriel, Gabriel, & Corthout, 1996; Gabriel, Lau, & Gabriel, 1996a, 1996b; Hancu et al., 2019; Mandija et al., 2021), various combinations of brain tissue conductivity values were assigned to the following tissues: cerebrospinal fluid (1.80–2.20 S/m with 0.10 step), white matter (0.30–0.45 S/m with 0.05 step), gray matter (0.50–0.65 S/m with 0.05 step). Additionally, to further increase the model complexity, cylindrical structures were included inside the head models mimicking lesions. For these cylindrical structures, different conductivity values were assigned: 0.60–1.60 S/m with 0.10 step (Hampe et al., 2020; Liao et al., 2019; Tha et al., 2014, 2018).

The simulated B_1^+ and B_1^- fields were then used for the synthetization of T2-w SE data (assuming $TR \gg T1 \gg TE$) as follows (Hoult, 2000; Katscher et al., 2013; Liu et al., 2017):

$$S(\alpha, \boldsymbol{r}) \approx V_1 M_0(\boldsymbol{r}) \cdot (1 - \exp(-TR/T1)) \cdot \exp(-TE/T2) \cdot H^-(\boldsymbol{r}) \cdot \exp(i\varphi^+(\boldsymbol{r})) \cdot \sin\left(V_2 \alpha |H^+(\boldsymbol{r})|\right) \quad (1)$$

where V_1 and V_2 correspond to system dependent constants, α is the flip angle, and $\boldsymbol{r}$ indicates space components: (x,y,z). H^+ and H^- are the circular polarized magnetic fields, corresponding to the RF transmit and receive fields, respectively. M_0 (Initial magnetization), which depends on relaxation effects and spin density, was utilized to mimic conventional T2-w MR contrast (Lu et al., 2005). The T2-w contrast synthetization parameters were set as follows; V_1 and $V_2 = 1$, flip angle = 90°, T1/T2: CSF = 4100/1700 ms, WM = 1100/60 ms, GM = 1600/80 ms; TR/TE: 4500/85 ms; M_0 ratio (CSF:WM:GM) = 1:0.7:0.8 (Lin et al., 2001; Sabati & Maudsley, 2013; Spijkerman et al., 2018; Stanisz et al., 2015). Additionally, the transceive phase was obtained as the sum of B_1^+ and B_1^- phase information (i.e., $\varphi^\pm = \varphi^+ + \varphi^-$). Then, the synthesized dataset was interpolated to match the target image parameters. Ultimately, the dataset composed of an approximated T2-w SE magnitude and transceive phase was generated for network training. The final image parameters of the synthesized T2-w data were FOV = 192 × 192 mm^2, image resolution = 1.0 × 1.0 mm^2, slice thickness = 2 mm, and the total number of the synthesized head models (consisting of approximated T2-w magnitude and transceive phase information) used for network training was 201 with their corresponding GTC pairs (for both Duke and Ella models). An example synthesized image can be seen in Figure 1.

2.2 | Data preparation

This section presents the data preparation steps, including augmentation of dataset and vectorization of input patches into the ANN (Figure 1, data processing and input parts).

Firstly, each synthesized T2-w SE magnitude image was multiplied by a random normalization factor n (0.7–1.3) to generate various intensity levels. Then, a random Gaussian noise $N(0,\gamma^2 I)$ was added to the real and imaginary components of the synthesized dataset ($n \cdot S$) targeting the actual T2-w in-vivo data SNR levels. We controlled the addition of noise to guarantee that the estimated decimal SNR level ranged from 15 to 25 in the white matter regions. This process can be expressed as follows:

$$S_{\text{noise}} = \left[\text{real}(n \cdot S) + N(0,\gamma^2 I)\right] + i\left[\text{imag}(n \cdot S) + N(0,\gamma^2 I)\right] \quad (2)$$

Secondly, the complex-valued S_{noise} data was converted to patched images with a stride step of one (in other words, in an 2D image space $R = (x,y)$, image patches can be extracted as $p = \left[\text{pixel}_{i-m:i+m}, \text{pixel}_{j-m:j+m} \mid i,j \in R\right]$) and split into synthesized T2-w SE magnitude and transceive phase information based on a patch size determination factor m (i.e., T2-w SE magnitude: $|S(p)|$; transceive phase: $\angle \text{S(p)}$). Since patched images for the transceive phase, which consists of two-dimensional parabolic components, include offsets, we shifted the patched phase value to have a minimum value of zero as a data normalization procedure. Finally, all the processed patches from both magnitude and phase data were vectorized to be fed into the developed network as input. The vectorized input of the ANN can be expressed as follow:

$$V_P = \left[\text{vec}(|S(p)|)', \text{vec}(\angle \text{S(p)})'\right]^T \text{where } S(p) = |S_{noise}(p)| \cdot \angle S_{noise}(\text{p}) \text{ in R} \quad (3)$$

This implies that the ANN input layer is connected to $2 \cdot (2 \cdot m + 1)^2$ input features generated from both magnitude and phase patches.

2.3 | Network training procedure

We built an ANN architecture containing three fully connected hidden layers attached with a rectifier linear unit (ReLU) and batch normalization. The number of neurons for these hidden layers was 1024, 512, and 512, respectively (Hornik, 1991). The input data are the iteratively new simulated noisy T2-w SE magnitude and transceive phase. The kernel size, 11 × 11 pixels (i.e., $m = 5$), was set empirically in consideration of the network performance and computational load.

In training, one single GTC label was assigned to each patch. This GTC label corresponds to the conductivity value of the pixel at the center of the input kernel. Thus, the output layer has only a single neuron attached with a sigmoid function. Adam optimizer (Kingma & Ba, 2015) was used for updating network parameters with a learning rate of 0.0001 and the model was trained for 500 epochs, with each epoch taking approximately 350 s. The mean-squared error between the label $\sigma(\text{pixel}_{i,j})$, and output $\text{ANN}(V_p)$ was utilized as a loss function:

$$\widehat{\sigma}(\text{pixel}_{i,j}) = \left\|\sigma(\text{pixel}_{i,j}) - \text{ANN}(V_p)\right\|_2^2 \quad (4)$$

The network was implemented using the Pytorch platform (Paszke et al., 2019). All of the ANN procedures were performed on a GPU workstation (GeForce GTX 1080 TI GPU; Nvidia, Santa Clara, CA) with an Intel Core I7-7500U at 2.70 GHz (Intel, Santa Cruz, CA).

2.4 | In-silico testing

In-silico tests were used to evaluate the performance of the proposed ANN-based reconstruction method since knowledge of GTC is available for the simulated data. All synthesized T2-w test datasets were generated based on rotationally augmented Ella datasets, which were excluded from the training dataset. The image parameters of the test datasets were the same as the training dataset, and Gaussian noise was added to the datasets mimicking realistic noise levels in clinical T2-w TSE data (SNR = 20). For comparison purposes, various 2D phase-based reconstruction methods, including Savitzky–Golay kernel (S-G kernel) + Gaussian filter with standard deviation (SD) = 1, magnitude weighted polynomial-fitting phase-based EPT (Poly-Fit method), and integral-based phase-based EPT (Integral-based method) were used (Karsa & Shmueli, 2021; Lee et al., 2016; Lee et al., 2015b).

In the first in-silico experiment, the rotationally augmented Ella head model (simulated rotation directions: x–y plane = 0°, x–z plane = 5°) with the following properties was used: CSF = 2.00 S/m, WM = 0.30 S/m, and GM = 0.50 S/m. Additional network (referred to as network A) was implemented for further investigation and comparison (Figure S1a). Network A had a single input channel comprised of transceive phase, while the GTC values were used as a label, similar to the proposed ANN-based reconstruction method. This network A was implemented to investigate whether the use of only the 2D transceive phase information as input would be sufficient for conductivity reconstructions, in contrast to the proposed network where both magnitude and phase information are provided.

In the second in-silico experiment, the proposed ANN-based method was tested on two rotationally augmented Ella head models with simulated lesions (cylindrical inclusions). The first model (simulated rotation directions: x–y plane = 5°, x–z plane = 0°) contained three inclusions with constant conductivity values (lesion 1: 0.80 S/m, lesion 2: 0.90 S/m, and lesion 3: 1.20 S/m), while the second model (simulated rotation directions: x–y plane = 0°, x–z plane = 0°) had one inclusion with two compartments (lesion 1: 1.00 S/m, and lesion 2: 1.50 S/m). For all these inclusions, the same T2-w image intensity was used to avoid any direct correlation between signal intensity and lesion conductivity. ANN-based reconstructions were then compared to GTC values and conductivity reconstructions from Poly-Fit method and Integral-based methods.

In the third in-silico experiment, the correlation between signal intensity and the reconstructed conductivity values was further

investigated. For such analysis, we evaluated whether there could be any dependency between the reconstructed conductivity values in simulated lesions and the input signal intensity for the conductivity range 0.60–1.50 S/m and signal intensity range 0.10–1.00 a.u. (SNR level: 8–70) based on the reported conductivity values for brain lesions (Hampe et al., 2020; Liao et al., 2019; Tha et al., 2014, 2018).

2.5 | In-vivo testing

For in-vivo testing, the proposed method was tested on T2-w TSE datasets acquired using 3 T MR systems. The scans were performed under the approval of the local institutional review board (Yonsei University Gangnam Severance Hospital, IRB, no: 3-2022-0443). For all in-vivo datasets, the multi-channel receive (multi-RX) coil combination method (Kim et al., 2022) was performed as a coil combination method to approximate the transceive phase information from the clinical settings with the multi-RX head coil. In addition, since there is no knowledge of the ground-truth tissue conductivity values for in-vivo brain, conductivity values reconstructed using the Poly-Fit method (Lee et al., 2016) were used for comparison purposes.

In-vivo datasets were acquired from two healthy volunteers using a 3 T MRI scanner (Tim Trio, Siemens Healthineers) with a 16-channel RX mode head coil (3 T Head/Neck 20 MR Coil, with 16-channel used for the head). 2D TSE sequence scans were conducted with the following parameters; Healthy volunteer 1 data: TR/TE = 4500/85 ms, image resolution = 1.0 × 1.0 mm^2, slice thickness = 3.0 mm, and the number of signal averages (AVG) = 8, AVG = 1, and scan time = 7 m 51 s; Healthy volunteer 2 data: TR/TE = 4500/85 ms, image resolution = 1.0 × 1.0 mm^2, and slice thickness = 3.0 mm, AVG = 1, and scan time = 59 s.

For the first and second in-vivo experiments, AVG was performed eight times on healthy volunteer 1 data to investigate the network performance for various SNR levels (AVG = 1 + addictive Gaussian noise, 1, 4, and 8; SNR levels = 10, 20, 40, and 58) and repeatability (the eight acquisitions with AVG = 1). As the third in-vivo experiment, the network was tested for various brain slices on the second healthy volunteer (healthy volunteer 2 data).

For the fourth in-vivo experiment, three meningioma patient data scanned using a 3 T scanner (MR750, GE Healthcare) with a 12-channel RX mode head coil (3 T 16CH Head Neck Spine (HNS) Array MRI Coil, with 12-channel used for the head) were tested. 2D TSE sequence scans were conducted with the following parameters; TR/TE = 4363/95 ms, image resolution = 0.625 × 0.75 mm^2, slice thickness = 2.0 mm, and AVG = 1 and scan time = 6 m 42 s. The patient datasets were resized to 1.0 × 1.0 mm^2 to match the input image resolution for the network. Additionally, we investigated whether the reconstructed conductivity maps would be correlated only to the T2-weighted MR contrast information or whether phase information was also relevant for in-vivo conductivity reconstructions. For this purpose, an additional comparison network (referred to as network B) was implemented and tested on patient datasets. Such network B was trained to reconstruct conductivity maps from only the synthesized T2-w MR contrast images. Details of implementation information are summarized in Figure S1b.

3 | RESULTS

3.1 | In-silico testing

Figure 2 shows the result of the first in-silico experiment. When using only transceive phase information as the network input, the DL results

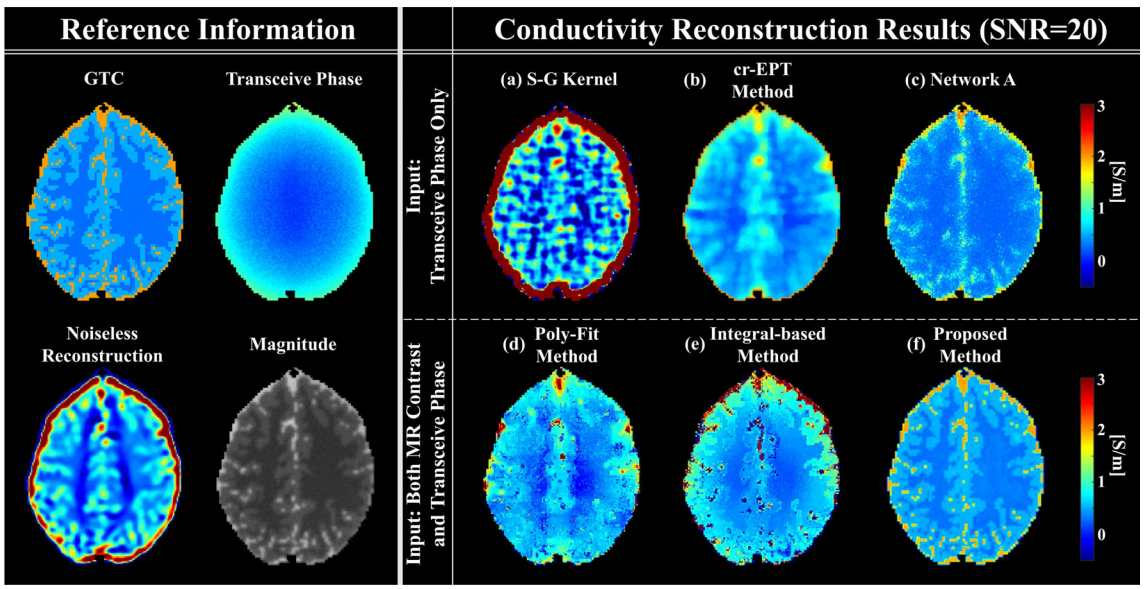

FIGURE 2 In-silico experiment 1. A brain simulation dataset was used to investigate conductivity reconstruction performance for four phase-based EPT reconstruction methods (a: S-G kernel, b: cr-EPT method, d: Poly-Fit method, e: Integral-based Method) and two neural networks (c: Network A, f: Proposed method) at SNR = 20. GTC, transceive phase, simplified Helmholtz phase-based EPT reconstruction under noiseless case, and magnitude information are shown on the left.

(Figure 2c, Network A) show that the networks can estimate the conductivity values with lower SD compared to the S-G kernel result (Figure 2a), but loss of structural information was still observed. As a further step, when both T2-w SE magnitude and transceive phase information were fed to the network as an input, tissue structural information was improved as shown in Figure 2f, proposed ANN method. In addition, the proposed method demonstrated better quality and more accurate conductivity reconstructions with lower SD values for each region of interest (ROI) inside the CSF, WM, and GM regions, compared to the conventional reconstruction methods (Figure 2b,d,e). The ROI analysis results are summarized in Table 1. The average processing time for one 2D slice head image with a 192 × 192 matrix was 0.19 s.

Figure 3 illustrates the results of the second in-silico experiment, demonstrating how the proposed method was able to distinguish the different conductivity values between lesions with the same T2-w signal intensity on the first head model (Figure 3: Head 1). Upon visual observation, the conventional phase-based EPT reconstruction methods (Figure 3a,b) were also able to differentiate the conductivity between these lesions. In addition, from the quantitative analysis (Table 2: Head 1), the mean and SD values for each lesion show that the proposed method can reconstruct conductivity values with more accuracy and precision than the conventional reconstruction methods.

Additionally, as shown from the results on the second head model characterized by a lesion with two compartments with different conductivity values but same T2-w signal intensity (Figure 3: Head 2), the proposed method can better reconstruct these two areas distinctively compared to conventional reconstructions. While the conventional reconstruction methods show the small contrast between the two area inside the lesion, the proposed method can define these areas with improved distinction. The more accurate mean and SD values obtained with the proposed method for each ROI also support these observations (Table 2: Head 2).

Figure 4 illustrates the dependency of the proposed network on the input signal intensity in the simulated lesions (in-silico experiment 3). As shown in the figure, the reconstructed conductivity values are minimally affected by changes in the input signal intensities, demonstrating that the network did not learn a painting procedure from magnitude signal to conductivity values. Ultimately, a slight overestimation occurred for very low (0.00–0.20 a.u.) or high (0.80–1.00 a.u.) signal intensities.

TABLE 1 ROI analysis result for the in-silico experiment 1.

	Mean (SD) [S/m]		
	CSF	WM	GM
GTC	2.00 (–)	0.30 (–)	0.50 (–)
S-G kernel	2.47 (9.04)	0.38 (1.12)	0.67 (1.37)
cr-EPT method	1.56 (0.24)	0.34 (0.10)	0.64 (0.21)
Network A	1.38 (0.58)	0.29 (0.05)	0.46 (0.18)
Poly-Fit method	1.75 (3.10)	0.37 (0.36)	0.60 (0.48)
Integral-based method	2.56 (2.31)	0.39 (0.12)	0.68 (0.33)
Proposed method	1.97 (0.20)	0.33 (0.04)	0.52 (0.08)

3.2 | Result for in-vivo testing

The first in-vivo experiment results on a healthy subject with various SNR levels (i.e., SNR = 10, 20, 40, and 58) are shown in Figure 5. The proposed method is more robust than the conventional method in preserving structural information for each SNR level. Additionally, the proposed method appears more noise robust as indicated by the lower SD values compared to the conventional reconstruction method Poly-Fit. Ultimately, the reconstructed averaged conductivity values in the adopted ROI are in good agreement with reported

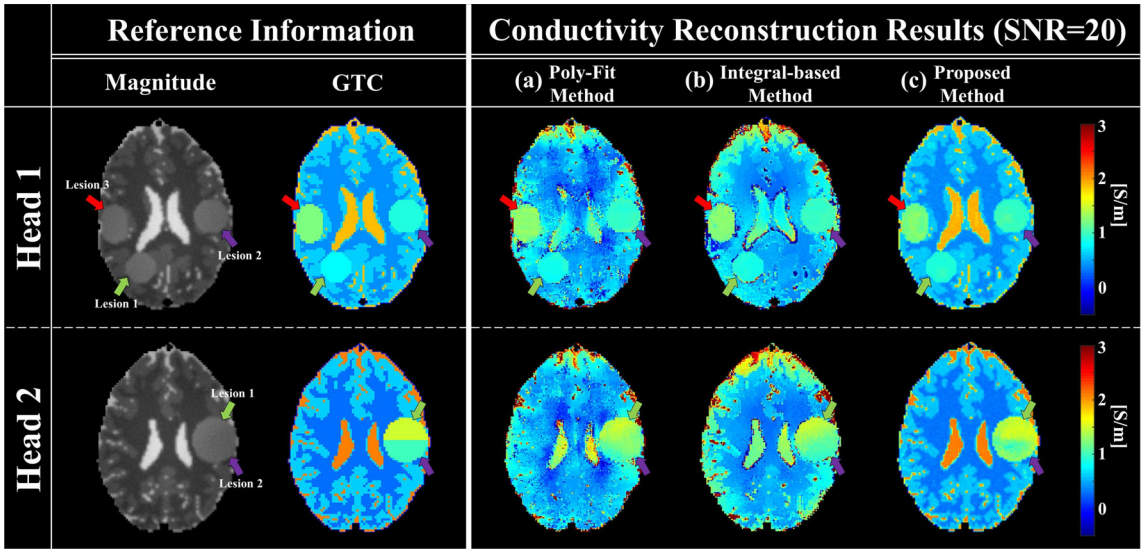

FIGURE 3 In-silico experiment 2: two test datasets with different simulated lesions. Comparison between two phase-based EPT reconstruction methods (a: Poly-Fit method, b: Integral-based method) and the proposed network (c: Proposed method).

TABLE 2 ROI analysis result for the in-silico experiment 2.

	Mean (SD) [S/m]					
	CSF	WM	GM	Lesion 1	Lesion 2	Lesion 3
Head 1						
GTC	1.90 (–)	0.40 (–)	0.60 (–)	0.80 (–)	0.90 (–)	1.20 (–)
Poly-Fit method	1.35 (1.64)	0.44 (0.40)	0.65 (0.54)	0.85 (0.12)	0.96 (0.11)	1.25 (0.18)
Integral-based method	1.38 (1.46)	0.47 (0.17)	0.73 (0.41)	0.86 (0.04)	0.98 (0.09)	1.22 (0.15)
Proposed method	1.94 (0.29)	0.37 (0.05)	0.58 (0.06)	0.82 (0.05)	0.93 (0.07)	1.18 (0.08)
Head 2						
GTC	2.10 (–)	0.30 (–)	0.60 (–)	1.00 (–)	1.50 (–)	– (–)
Poly-Fit method	1.66 (2.11)	0.40 (0 35)	0.66 (0.50)	1.15 (0.22)	1.39 (0.35)	– (–)
Integral-based method	1.74 (1.92)	0.41 (0.17)	0.82 (0.35)	1.18 (0.19)	1.33 (0.12)	– (–)
Proposed method	2.13 (0.13)	0.32 (0.03)	0.57 (0.05)	1.07 (0.14)	1.51 (0.08)	– (–)

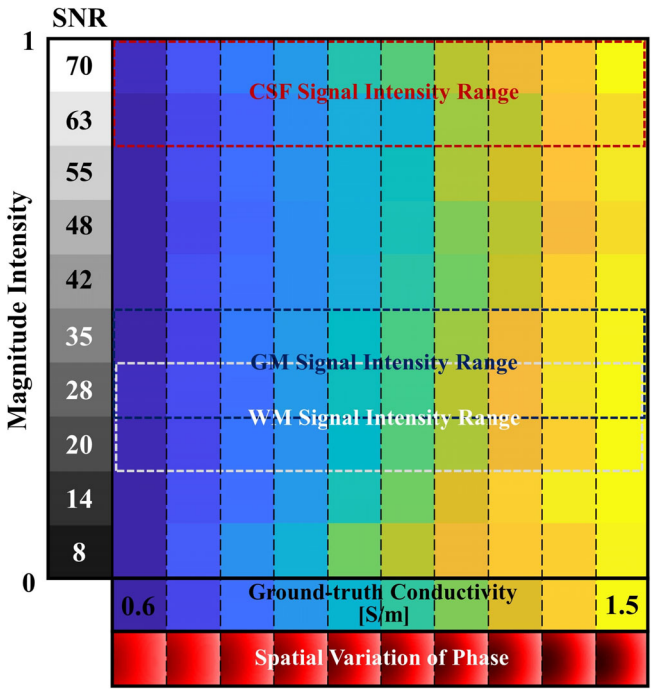

FIGURE 4 In-silico experiment 3. Reconstructed conductivity values for different magnitude signal intensity and conductivity combinations (Note that SNR level index is plotted inside the reference color index for magnitude signal intensity). The results show that the output of the proposed network is minimally affected by input magnitude signal values.

literature brain conductivity values in healthy subjects (Gabriel, Gabriel, & Corthout, 1996; Gabriel, Lau, & Gabriel, 1996a, 1996b; Hancu et al., 2019; Mandija et al., 2021), although they appear slightly lower than the values computed using the Poly-Fit method, used here as a second independent reference. ROI analysis results are summarized in Table 3, and the corresponding tissue segmentation information is shown in Figure S2.

The second in-vivo experiment results on the repeatability of conductivity reconstructions are shown in Figure 6. As seen Figure 6a, the Poly-Fit reconstructions seem more unstable compared to the proposed method between each scan. Magnitude and phase data showed a strong positive correlation among the repeated scans (Figure 6b left). The reconstructed conductivity maps with the conventional method (Poly-Fit method) showed a moderate positive correlation with inconsistent values (coefficient SD = 0.037), whereas the proposed method showed much higher and strong positive correlation (coefficient SD = 0.005) between each scan (Figure 6b right). A factor that affects the repeatability experiment of conductivity reconstructions is the variation of the phase as shown in the zoom-in part of the phase maps (Figure 6a).

While defected contrast information is not observed in T2-w magnitude images, differences in the reconstructed conductivity values are revealed with respect to two groups of different phase distributions among the different repetitions. Areas with overall underestimated values (yellow box) and overestimated values (red box) are indicated. These differences are more evident for the conventional Poly-Fit method used here as a reference.

The third in-vivo experiment shows conductivity reconstructions on a second healthy subject on different brain slices (Figure 7). The results illustrate consistent conductivity values in the WM, GM, and CSF across slices, demonstrating the capability of the proposed method to reconstruct conductivity maps for various brain slices from T2-w TSE dataset.

Figure 8 shows the result on three meningioma patients. In this figure, the reconstructions using the network B are also included for comparison purposes. As shown in Figure 8b,d, the difference between the proposed method and the network B (reconstruction of conductivity maps from only T2-w magnitude intensity information) was noticeable, especially in WM and lesion regions. In addition, the WM inhomogeneity was observed in the T2-w images for patients 1 and 3 (Figure 8a), the network B was significantly affected by the MR contrast and showed defective results, while this was not observed using the proposed network. Furthermore, as illustrated in Figure 8d, the proposed method shows sharper boundaries, making a distinction between tissue structures better visible compared to the other methods. Quantitative comparison for the reconstructed

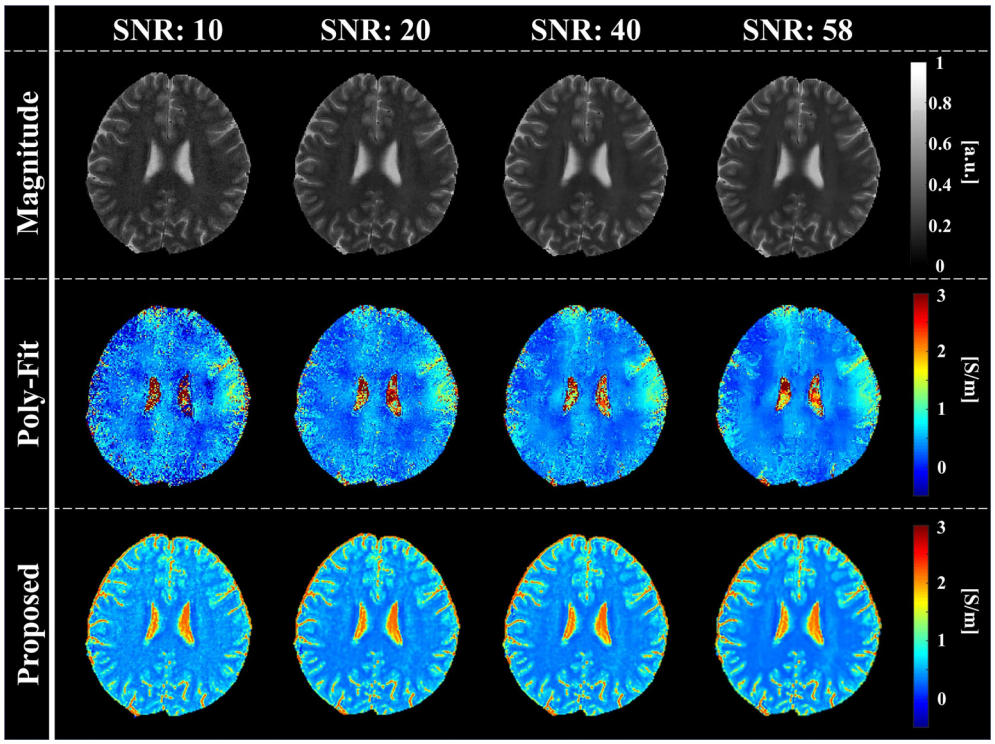

FIGURE 5 In-vivo experiment 1: conductivity reconstructions on a healthy volunteer for various SNR levels (Healthy volunteer data 1) for the proposed method (bottom line) and the reference Poly-Fit method (middle line).

TABLE 3 ROI analysis result for the first in-vivo experiment.

	Mean (SD) [S/m]		
	CSF	WM	GM
Poly-Fit method			
SNR 10	2.47 (4.95)	0.36 (0.38)	0.62 (2.52)
SNR 20	2.10 (2.54)	0.36 (0.28)	0.63 (1.61)
SNR 40	2.09 (1.14)	0.37 (0.19)	0.65 (1.24)
SNR 58	2.11 (0.98)	0.37 (0.17)	0.63 (1.09)
Proposed method			
SNR 10	1.93 (0.45)	0.40 (0.08)	0.62 (0.26)
SNR 20	1.95 (0.39)	0.34 (0.06)	0.61 (0.25)
SNR 40	1.95 (0.38)	0.34 (0.06)	0.61 (0.25)
SNR 58	1.95 (0.37)	0.33 (0.05)	0.61 (0.23)

conductivity values in the lesions using the conventional reconstruction method (Poly-Fit method) and the proposed method is also shown in Figure 8. The measured mean and SD values over each patient's lesion were as follows; Patient 1: Poly-Fit = 0.84 (0.70) S/m, Proposed = 0.80 (0.38) S/m; Patient 2: Poly-Fit = 0.69 (0.29) S/m, Proposed = 0.74 (0.20) S/m; Patient 3: Poly-Fit = 0.99 (0.26) S/m, Proposed = 0.97 (0.18) S/m.

4 | DISCUSSION

In this work, we implemented a 2D patch-based non-linear conductivity estimator for T2-w SE images by training an ANN using phase maps from FDTD simulations at 3 T and synthetic T2-w magnitude maps with 1×1 mm^2 resolutions. The in-silico experiments demonstrated the capability of the proposed method to accurately reconstruct conductivity values in a pixel-wise manner while preserving the tissue structural information in contrast to conventional methods, which suffer from errors at tissue boundaries and noise amplification in the reconstructed conductivity maps. The in-vivo experiments showed that the proposed network, which was trained only on the simulated dataset, can provide good-quality conductivity maps at various SNR levels, demonstrating its noise robustness. Furthermore, the repeatability experiment using in-vivo data demonstrated that the proposed method could produce almost consistent conductivity maps with revealing phase distributions from data acquired multiple times using the same MRI acquisition (i.e., $8 \times$ AVG = 1 T2-w TSE datasets) (Arduino et al., 2023). We applied our proposed method to three meningioma patients. The preliminary investigations suggest that the network trained on simulated data may distinguish and characterize pathological tissues. Previously, it has been shown that tissue stiffness can be different depending on the hardness and heterogeneity of the meningiomas in magnetic resonance elastography images (Hughes et al., 2015). Given the different tissue structures and compositions, conductivity values may also differ for different tumor stiffness. This was our main motivation to investigate the proposed method on meningioma patients. In this study, we observed characteristics and distribution of the conductivity for meningioma cases, which were classified into the following two groups: tumors with soft consistency (Patients 1 and 3) and tumors with hard consistency (Patient 2). As an initial observation, it was seen that the soft consistency tumors had a higher conductivity than the hard consistency tumor. However, since this was investigated on only three patients

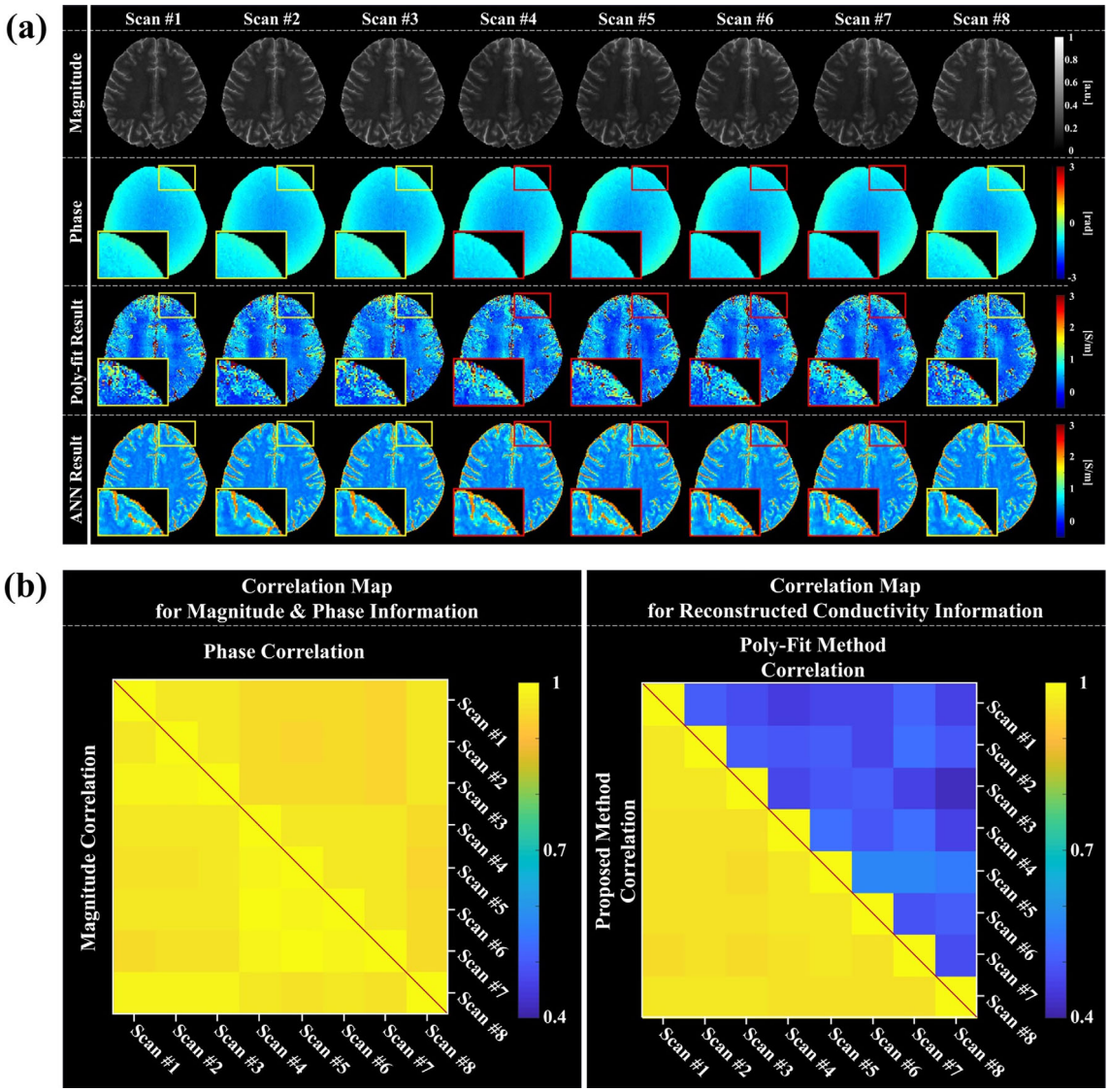

FIGURE 6 In-vivo experiment 2: repeatability (Healthy volunteer data 1). (a) The eight individual conductivity reconstructions are shown. Note the variations in the conductivity (e.g., boxed-area). Yellow box indicates estimated conductivity, and red box indicates underestimated conductivity. (b) correlation maps between the eight scans, (left) magnitude and phase data correlation showing very small changes, (right) reconstructed conductivity maps correlation showing larger variations for the Poly-Fit method with respect to the proposed method.

with meningioma, further validation is needed from a large amount of patient datasets with various lesions to validate and demonstrate the diagnostic capability of the proposed approach.

To solve the full Helmholtz equation for conductivity reconstructions, not only B_x and B_y but also B_z information is required. However, in conventional MRI settings, only partial information B_x and B_y is available. Such restriction leads to rely on the simplified Helmholtz equation with certain assumptions (i.e., piece-wise constant assumption and negligible B_z assumption) for the observations of EPs maps from in-vivo dataset. Here, we used the B-map simulations in the training dataset to take into account these restrictions.

Based on the simulation dataset, we used a rather simple ANN architecture to perform conductivity reconstruction. In general, DL models can intentionally apply inductive bias to achieve better performance on specific datasets (Battaglia et al., 2018). Especially, in the convolutional neural network (CNN) based approaches mostly applied in the DL studies for EPT (Gavazzi et al., 2020; Hampe et al., 2020; Inda et al., 2022; Jung, Lee, et al., 2021; Jung, Mandija, et al., 2021; Leijsen et al., 2022; Mandija et al., 2019), the spatial feature extraction process using convolutional layers may introduce such inductive bias even with a small training dataset (Lecun et al., 1998; Ronneberger et al., 2015; Ulyanov et al., 2020). However, if the inductive bias is designed to be inappropriate or too strong, the trained model can lead to a poor variance with spurious results, subsequently degrading generalization performance. The trade-off between inductive bias and generalization performance should be handled carefully (Battaglia

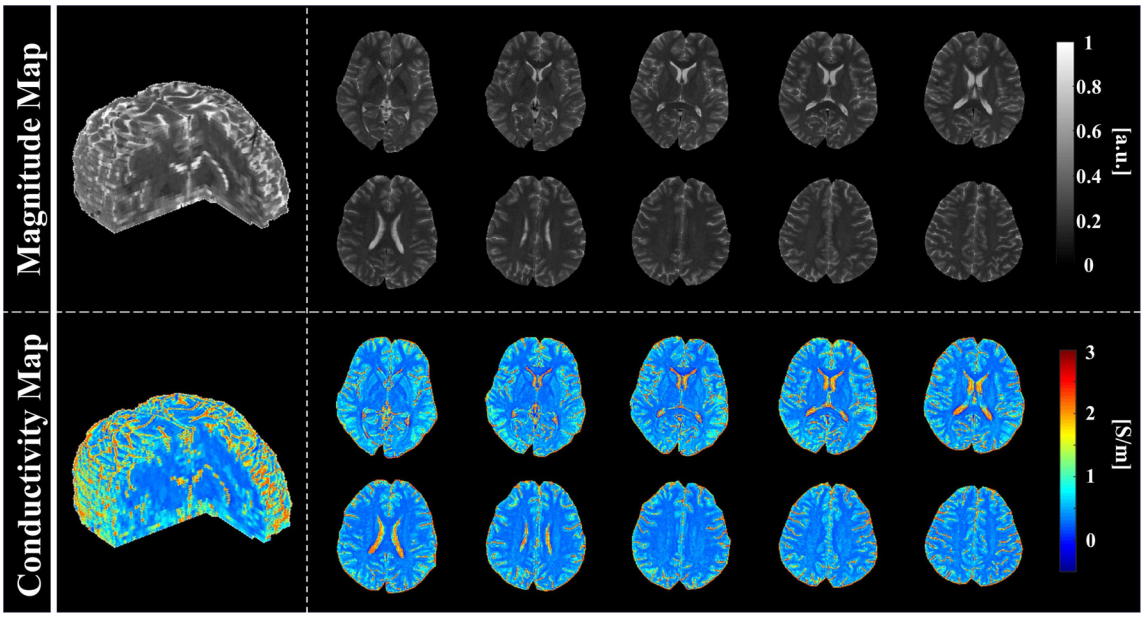

FIGURE 7 In-vivo experiment 3: reconstructed conductivity over the whole brain volume (Healthy volunteer data 2). The magnitude image and its corresponding conductivity are shown over multiple slices.

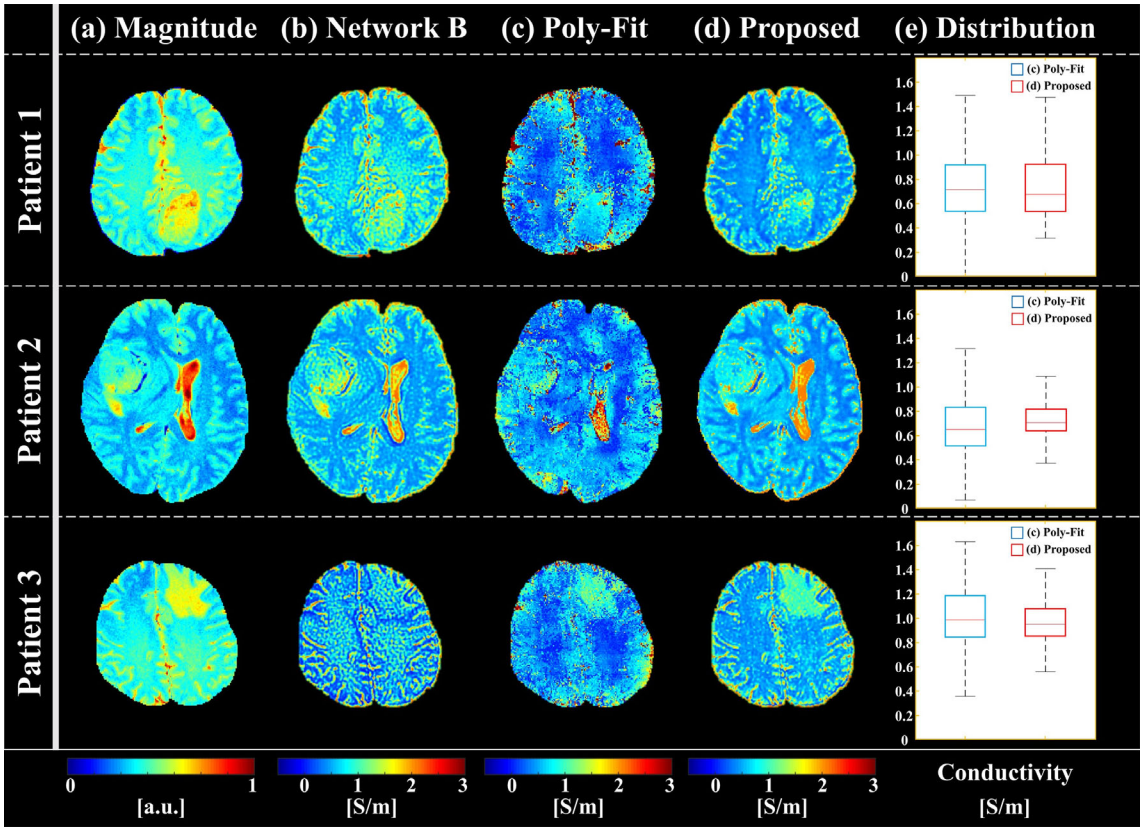

FIGURE 8 In-vivo experiment 4 for three patient datasets. In each lesion, the estimated conductivity distribution was compared between results for Poly-Fit and proposed method. (a) T2-w magnitude images, (b) Network B, (c) Poly-Fit reconstruction result, (d) Proposed method result, (e) Box & Whisker plot over lesions areas.

et al., 2018). Motivated by these observations, a multi-layer perceptron (MLP) has been taken notice again with its characteristics where all weights are independent and not shared (Battaglia et al., 2018; Liu et al., 2021). Thus, if a large number of physics-coupled datasets can be constructed, ANN may also be an efficient estimation solver to tackle various non-linear computation problems.

The proposed network was implemented based on a pixel-wise estimation approach, and it also demonstrated the significance of providing MR contrast information into the network for better resolving of tissue boundaries. As observed in Figure 2c,f, the additional T2-w magnitude image acts as a regularization factor in the network for conductivity estimations, and this implicit regularization has been learned by the network via T2-w images. As shown in Figures 4 and 5, the implicit regularization exhibited the ability to discriminate against the potential issue where the T2-w magnitude images exhibit a homogeneity, yet the conductivity properties may possess in variations (Note that too high or low magnitude intensities tend to be overestimated). In addition, in Figure 8, the results for the proposed method and the network B suggest that the network effectively utilizes transceive phase information along with the implicit regularization from T2-w magnitude information. Notably, distinct differences were observed in the pathological regions and WM with hyperintense regions (Patients 1 and 3). Alternative contrast images such as T1-w and PD-w could likewise be used for training.

The proposed method may be affected by various confounding factors, such as B_1 inhomogeneities, noise, motion, and vessel pulsation. Although the proposed method is expected to be more robust to such factors compared to the conventional phase-based EPT reconstruction methods (Lee et al., 2021), the experiment results show that noise still impairs the estimation accuracy (Figure 5), and changes in the phase distribution are reflected in the conductivity estimations for the in-vivo dataset (Figures 6 and 8). Thus, it would be worthwhile to investigate the combination of various artifact reduction or denoising algorithms (Cui et al., 2022; Jung, Mandija, et al., 2021; Michel et al., 2014) with the proposed method to improve the estimation performance for datasets affected by artifacts or high noise.

This method has the following limitations. Firstly, since the proposed method was implemented by targeting the network using one specific MR contrast (i.e., T2-w images), the network may perform improperly for other contrast-weighted images. Using tissue segmentation instead of magnitude contrast information may allow the proposed method to generalize with respect to the image contrast (Ashburner & Friston, 2005; Karsa & Shmueli, 2021; Shattuck & Leahy, 2002; Smith et al., 2004). Secondly, the proposed method was implemented based on the premise of the transceive phase assumption. Since the transceive phase assumption typically holds for birdcage coils, in this study, the transceive phase was approximated from the multi-RX coil by using the multi-RX combination method (Kim et al., 2022). Although the use of birdcage coils may facilitate access to transceive phase information, multi-RX coils may be preferred in clinical settings for SNR or compatibility with parallel imaging techniques. However, the use of a multi-RX coil may still be a factor that could affect the estimation performance of the proposed method. Therefore, as a future study, if a simulation environment can be constructed to match the coil configuration used in actual clinical settings, the performance of the proposed method could be improved. In addition, it may not be directly applicable to ultra-high field systems where the wavelength of the RF pulse is shortened (e.g., 7 and 9.4 T). Thirdly, ground-truth conductivity information was not available for in-vivo cases. Thus, we could not accurately evaluate the reconstruction capability of the proposed method in-vivo. Here, we compared conductivity maps with reported literature values and alternative conventional methods. We observed that the reconstructed conductivity values in the WM, GM, and CSF tissue are in line with reported literature values. Further investigations should be performed using realistic brain phantoms with knowledge of GTC information (Meerbothe et al., 2022).

Recently, several studies have been conducted to further ensure network reliability. As a future study, uncertainty estimations could be added to the proposed method (Gal & Ghahramani, 2016; Glang et al., 2020; Jung et al., 2022; Roy et al., 2019; Tanno et al., 2021), thus evaluating network instability, for example, by employing dropout with Bayesian approximation. As another option, physics-informed networks (Inda et al., 2022; Lim & Psaltis, 2022; Raissi et al., 2019; Yu et al., 2023) can be considered. Nevertheless, since B_z information is required to solve the full Helmholtz equation, it may still be difficult to apply the method in practice for phase-based EPT reconstruction algorithms. Thus, for applications, it would be worthwhile to investigate the methods of composing the physics-driven loss by (1) utilizing modified equations with their underlying assumptions (e.g., piece-wise assumption or neglecting B_z component), (2) partially combining the network with the physics equation included in estimating B_z (Eda et al., 2022; Guo et al., 2017), or (3) applying iterative integral based EPs estimation methods (Balidemaj et al., 2015b; Giannakopoulos et al., 2021).

5 | CONCLUSIONS

In summary, we proposed an ANN-based method to reconstruct conductivity maps in a pixel-wise manner using only simulated data in the training procedure. The results show accurate and good-quality reconstructions in-silico. In addition, the estimated in-vivo brain conductivity maps suggest the feasibility of directly applying this method to in-vivo volunteer and meningioma patient data. Finally, the proposed method can potentially be applied to patient data whose conductivity values are known to change.

ACKNOWLEDGMENTS

This work was supported by the National Research Foundation of Korea (NRF) grant funded by the Korea government (MSIT) (No. NRF-2022R1A4A1030579) and by the MSIT(Ministry of Science and ICT), Korea, under the ITRC (Information Technology Research Center) support program (IITP-2022-2020-0-01461) supervised by the IITP (Institute for Information & Communications Technology Planning & Evaluation). Stefano Mandija received funding from Netherlands Organisation for Scientific Research (NWO), VENI grant number: 18078.

CONFLICT OF INTEREST STATEMENT

The authors have declared that there is no conflict of interest.

DATA AVAILABILITY STATEMENT

The code supporting the findings of this study is openly available at https://github.com/Yonsei-MILab/Non-linear-Conductivity-Estimator. Due to the use of the commercial FDTD software (Sim4Life) with two commercial head models (Duke and Ella) to compute electromagnetic fields in this study, the simulation dataset cannot be shared. As an alternative, an example dataset with synthesized cylinder models, which was computed by the Bessel-boundary-matching method (van den Bergen et al., 2009), is provided.

ORCID

Kyu-Jin Jung https://orcid.org/0000-0003-2842-1707
Stefano Mandija https://orcid.org/0000-0002-4612-5509
Chuanjiang Cui https://orcid.org/0009-0009-8927-8271
Jun-Hyeong Kim https://orcid.org/0000-0001-8382-0589
Mohammed A. Al-masni https://orcid.org/0000-0002-1548-965X
Thierry G. Meerbothe https://orcid.org/0009-0009-5736-1038
Mina Park https://orcid.org/0000-0002-2005-7560
Cornelis A. T. van den Berg https://orcid.org/0000-0002-5565-6889
Dong-Hyun Kim https://orcid.org/0000-0002-6717-7770

REFERENCES

Arduino, A., Pennecchi, F., Katscher, U., Cox, M., & Zilberti, L. (2023). Repeatability and reproducibility uncertainty in magnetic resonance-based electric properties tomography of a homogeneous phantom. *Tomography*, *9*(1), 420–435.

Ashburner, J., & Friston, K. J. (2005). Unified segmentation. *NeuroImage*, *26*(3), 839–851.

Balidemaj, E., De Boer, P., Van Lier, A. L., Remis, R. F., Stalpers, L. J. A., Westerveld, G. H., Nederveen, A. J., Van Den Berg, C. A. T., & Crezee, J. (2016). In vivo electric conductivity of cervical cancer patients based on maps at 3T MRI. *Physics in Medicine & Biology*, *61*(4), 1596–1607.

Balidemaj, E., van den Berg, C. A. T., Trinks, J., van Lier, A. L. H. W., Nederveen, A. J., Stalpers, L. J. A., Crezee, H., & Remis, R. F. (2015b). CSI-EPT: A contrast source inversion approach for improved MRI-based electric properties tomography. *IEEE Transactions on Medical Imaging*, *34*(9), 1788–1796.

Balidemaj, E., van den Berg, C. A. T., van Lier, A. L. H. M. W., Nederveen, A. J., Stalpers, L. J. A., Crezee, H., & Remis, R. F. (2017). B1-based SAR reconstruction using contrast source inversion–electric properties tomography (CSI-EPT). *Medical & Biological Engineering & Computing*, *55*(2), 225–233.

Balidemaj, E., van Lier, A. L. M. W., Crezee, H., Nederveen, A. J., Stalpers, L. J. A., & van den Berg, C. A. T. (2015a). Feasibility of electric property tomography of pelvic tumors at 3T. *Magnetic Resonance in Medicine*, *73*(4), 1505–1513.

Battaglia, P. W., Hamrick, J. B., Bapst, V., Sanchez-Gonzalez, A., Zambaldi, V., Malinowski, M., Tacchetti, A., Raposo, D., Santoro, A., Faulkner, R., Gulcehre, C., Song, F., Ballard, A., Gilmer, J., Dahl, G., Vaswani, A., Allen, K., Nash, C., Langston, V., … Pascanu, R. (2018). Relational inductive biases, deep learning, and graph networks. *arXiv Preprint arXiv:1806.01261*.

Baymani, M., Effati, S., Niazmand, H., & Kerayechian, A. (2015). Artificial neural network method for solving the Navier–Stokes equations. *Neural Computing and Applications*, *26*(4), 765–773.

Ben-Shabat, Y., & Gould, S. (2020). Deepfit: 3D surface fitting via neural network weighted least squares. *Proceedings of European Conference on Computer Vision*, 16, 20–34.

Chakraverty, S., & Mall, S. (2020). Single layer Chebyshev neural network model with regression-based weights for solving nonlinear ordinary differential equations. *Evolutionary Intelligence*, *13*, 687–694.

Christ, A., Kainz, W., Hahn, E. G., Honegger, K., Zefferer, M., Neufeld, E., Rascher, W., Janka, R., Bautz, W., Chen, J., Kiefer, B., Schmitt, P., Hollenbach, H. P., Shen, J., Oberle, M., Szczerba, D., Kam, A., Guang, J. W., & Kuster, N. (2009). The virtual family—Development of surface-based anatomical models of two adults and two children for dosimetric simulations. *Physics in Medicine & Biology*, *55*(2), N23–N38.

Cui, C., Kim, J. H., Jung, K. J., Yi, J., & Kim, D. H. (2022). Deep prior for suppressing noise amplification and edge preservation in phase-based EPT with low-SNR image. *Proceedings of the International Society for Magnetic Resonance in Medicine*, *2914*.

Duan, S., Xu, C., Deng, G., Wang, J., Liu, F., & Xin, S. X. (2016). Quantitative analysis of the reconstruction errors of the currently popular algorithm of magnetic resonance electrical property tomography at the interfaces of adjacent tissues. *NMR in Biomedicine*, *29*(6), 744–750.

Eda, N., Fushimi, M., Hasegawa, K., & Nara, T. (2022). A method for electrical property tomography based on a three-dimensional integral representation of the electric field. *IEEE Transactions on Medical Imaging*, *41*(6), 1400–1409.

Gabriel, C., Gabriel, S., & Corthout, E. (1996). The dielectric properties of biological tissues: I. Literature survey. *Physics in Medicine & Biology*, *41*(11), 2231–2249.

Gabriel, S., Lau, R. W., & Gabriel, C. (1996a). The dielectric properties of biological tissues: II. Measurements in the frequency range 10 Hz to 20 GHz. *Physics in Medicine & Biology*, *41*(11), 2251–2269.

Gabriel, S., Lau, R. W., & Gabriel, C. (1996b). The dielectric properties of biological tissues: III. Parametric models for the dielectric spectrum of tissues. *Physics in Medicine & Biology*, *41*(11), 2271–2293.

Gal, Y., & Ghahramani, Z. (2016). Dropout as a Bayesian approximation: Representing model uncertainty in deep learning. *Proceedings of International Conference on Machine Learning*, *48*, 1050–1059.

Gavazzi, S., van den Berg, C. A. T., Savenije, M. H. F., Kok, H. P., de Boer, P., Stalpers, L. J. A., Lagendijk, J. J. W., Crezee, H., & van Lier, A. L. H. M. W. (2020). Deep learning-based reconstruction of in vivo pelvis conductivity with a 3D patch-based convolutional neural network trained on simulated MR data. *Magnetic Resonance in Medicine*, *84*(5), 2772–2787.

Giannakopoulos, I. I., Serrallés, J. E. C., Daniel, L., Sodickson, D. K., Polimeridis, A. G., White, J. K., & Lattanzi, R. (2021). Magnetic-resonance-based electrical property mapping using global Maxwell tomography with an 8-channel head coil at 7 Tesla: A simulation study. *IEEE Transactions on Biomedical Engineering*, *68*(1), 236–246.

Glang, F., Deshmane, A., Prokudin, S., Martin, F., Herz, K., Lindig, T., Bender, B., Scheffler, K., & Zaiss, M. (2020). DeepCEST 3T: Robust MRI parameter determination and uncertainty quantification with neural networks—Application to CEST imaging of the human brain at 3T. *Magnetic Resonance in Medicine*, *84*(1), 450–466.

Gosselin, M. C., Neufeld, E., Moser, H., Huber, E., Farcito, S., Gerber, L., Jedensjö, M., Hilber, I., Di Gennaro, F., Lloyd, B., Cherubini, E., Szczerba, D., Kainz, W., & Kuster, N. (2014). Development of a new generation of high-resolution anatomical models for medical device evaluation: The virtual population 3.0. *Physics in Medicine & Biology*, *59*(18), 5287–5303.

Guo, L., Jin, J., Liu, C., Liu, F., & Crozier, S. (2017). An efficient integral-based method for three-dimensional MR-EPT and the calculation of the RF-coil-induced Bz field. *IEEE Transactions on Biomedical Engineering*, *65*(2), 282–293.

Gurler, N., & Ider, Y. Z. (2017). Gradient-based electrical conductivity imaging using MR phase. *Magnetic Resonance in Medicine*, *77*(1), 137–150.

Haacke, E. M., Petropoulos, L. S., Nilges, E. W., & Wu, D. H. (1991). Extraction of conductivity and permittivity using magnetic resonance imaging. *Physics in Medicine & Biology*, *36*(6), 723–734.

Hafalir, F. S., Oran, O. F., Gurler, N., & Ider, Y. Z. (2014). Convection-reaction equation based magnetic resonance electrical properties tomography (cr-MREPT). *IEEE Transactions on Medical Imaging*, *33*(3), 777–793.

Hampe, N., Katscher, U., van den Berg, C. A. T., Tha, K. K., & Mandija, S. (2020). Investigating the challenges and generalizability of deep learning brain conductivity mapping. *Physics in Medicine & Biology*, *65*(13), 135001.

Hancu, I., Liu, J., Hua, Y., & Lee, S. K. (2019). Electrical properties tomography: Available contrast and reconstruction capabilities. *Magnetic Resonance in Medicine*, *81*(2), 803–810.

Hong, R., Li, S., Zhang, J., Zhang, Y., Liu, N., Yu, Z., & Liu, Q. H. (2017). 3-D MRI-based electrical properties Tomogarphy using the volume integral equation method. *IEEE Transactions on Microwave Theory and Techniques*, *65*(12), 4802–4811.

Hornik, K. (1991). Approximation capabilities of multilayer feedforward networks. *Neural Networks*, *4*(2), 251–257.

Hoult, D. I. (2000). The principle of reciprocity in signal strength calculations—A mathematical guide. *Concepts in Magnetic Resonance: An Educational Journal*, *12*(4), 173–187.

Hughes, J. D., Fattahi, N., Van Gompel, J., Arani, A., Meyer, F., Lanzino, G., Link, M. J., Ehman, R., & Huston, J. (2015). Higher-resolution magnetic resonance elastography in meningiomas to determine intratumoral consistency. *Neurosurgery*, *77*(4), 653–659.

Inda, A. J. G., Huang, S. Y., İmamoğlu, N., & Yu, W. (2022). Physics-coupled neural network magnetic resonance electrical property tomography (MREPT) for conductivity reconstruction. *IEEE Transactions on Image Processing*, *31*, 3463–3478.

Jung, K. J., Mandija, S., Kim, J. H., Ryu, K., Jung, S., Cui, C., Kim, S. Y., Park, M., van den Berg, C. A., & Kim, D. H. (2021). Improving phase-based conductivity reconstruction by means of deep learning–based denoising of phase data for 3T MRI. *Magnetic Resonance in Medicine*, *86*(4), 2084–2094.

Jung, S., Lee, H., Ryu, K., Song, J. E., Park, M., Moon, W. J., & Kim, D. H. (2021). Artificial neural network for multi-echo gradient echo-based myelin water fraction estimation. *Magnetic Resonance in Medicine*, *85*(1), 380–389.

Jung, S., Yun, J. S., Kim, D. Y., & Kim, D. H. (2022). Improved multi-echo gradient echo myelin water fraction mapping using complex-valued neural network analysis. *Magnetic Resonance in Medicine*, *88*(1), 492–500.

Karsa, A., Fuchs, P., & Shmueli, K. (2021). Optimal kernel radii for calculating the derivatives of Noisy B1 phase for accurate phase-based quantitative conductivity mapping. *Proceedings of the International Society for Magnetic Resonance in Medicine*, *3775*.

Karsa, A., & Shmueli, K. (2021). New approaches for simultaneous noise suppression and edge preservation to achieve accurate quantitative conductivity mapping in Noisy images. *Proceedings of the International Society for Magnetic Resonance in Medicine*, *3774*.

Katscher, U., Gagiyev, M., & Meineke, J. (2016). Conductivity determination of deep gray matter nuclei utilizing susceptibility-based delineation. *Proceedings of the International Society for Magnetic Resonance in Medicine*, *3336*.

Katscher, U., Kim, D. H., & Seo, J. K. (2013). Recent progress and future challenges in MR electric properties tomography. *Computational and Mathematical Methods in Medicine*, *2013*, 1–11.

Katscher, U., Voigt, T., Findeklee, C., Vernickel, P., Nehrke, K., & Dössel, O. (2009). Determination of electric conductivity and local SAR via B1 mapping. *IEEE Transactions on Medical Imaging*, *28*(9), 1365–1374.

Kim, J. H., Shin, J., Jung, K. J., Cui, C., Kim, S. Y., Lee, J. H., & Kim, D. H. (2022). Multi-receiver combination method for phase-based electrical property tomography of the breast. *Medical Physics*, *50*(3), 1660–1669.

Kim, S. Y., Shin, J., Kim, D. H., Kim, M. J., Kim, E. K., Moon, H. J., & Yoon, J. H. (2016). Correlation between conductivity and prognostic factors in invasive breast cancer using magnetic resonance electric properties tomography (MREPT). *European Radiology*, *26*(7), 2317–2326.

Kingma, D. P., & Ba, J. (2015). Adam: A method for stochastic optimization. *Proceedings of the International Conference on Learning Representations* (pp. 1-15).

Kwon, K., Kim, D., & Park, H. W. (2017). A parallel MR imaging method using multilayer perceptron. *Medical Physics*, *44*(12), 6209–6224.

Lazebnik, M., Popovic, D., McCartney, L., Watkins, C. B., Lindstrom, M. J., Harter, J., Sewall, S., Ogilvie, T., Magliocco, A., Breslin, T. M., Temple, W., Mew, D., Booske, J. H., Okoniewski, M., & Hagness, S. C. (2007). A large-scale study of the ultrawideband microwave dielectric properties of normal, benign and malignant breast tissues obtained from cancer surgeries. *Physics in Medicine & Biology*, *52*(20), 6093–6115.

Lecun, Y., Bottou, L., Bengio, Y., & Haffner, P. (1998). Gradient-based learning applied to document recognition. *Proceedings of the IEEE*, *86*(11), 2278–2324.

Lee, J., Shin, J., & Kim, D. H. (2016). MR-based conductivity imaging using multiple receiver coils. *Magnetic Resonance in Medicine*, *76*(2), 530–539.

Lee, J. H., Yoon, Y. C., Kim, H. S., Lee, J., Kim, E., Findeklee, C., & Katscher, U. (2022). In vivo electrical conductivity measurement of muscle, cartilage, and peripheral nerve around knee joint using MR-electrical properties tomography. *Scientific Reports*, *12*(73), 1–10.

Lee, M. B., Jahng, G. H., Kim, H. J., & Kwon, O. I. (2021). High-frequency conductivity at Larmor-frequency in human brain using moving local window multilayer perceptron neural network. *PLoS One*, *16*(5), e0251417.

Lee, S. K., Bulumulla, S., Wiesinger, F., Sacolick, L., Sun, W., & Hancu, I. (2015a). Tissue electrical property mapping from zero echo-time magnetic resonance imaging. *IEEE Transactions on Medical Imaging*, *34*(2), 541–550.

Lee, S. K., Bulumulla, S., & Hancu, I. (2015b). Theoretical investigation of random noise-limited signal-to-noise ratio in MR-based electrical properties tomography. *IEEE Transactions on Medical Imaging*, *34*(11), 2220–2232.

Leijsen, R., van den Berg, C., Webb, A., Remis, R., & Mandija, S. (2022). Combining deep learning and 3D contrast source inversion in MR-based electrical properties tomography. *NMR in Biomedicine*, *35*(4), e4211.

Liao, Y., Oros-Peusquens, A. M., Lindemeyer, J., Lechea, N., Weiß-Lucas, C., Langen, K. J., & Shah, N. J. (2019). An MR technique for simultaneous quantitative imaging of water content, conductivity and susceptibility, with application to brain tumours using a 3T hybrid MR-PET scanner. *Scientific Reports*, *9*(1), 1–12.

Lim, J., & Psaltis, D. (2022). MaxwellNet: Physics-driven deep neural network training based on Maxwell's equations. *APL Photonics*, *7*(1), 011301.

Lin, C., Bernstein, M., Huston, J., & Fain, S. (2001). *Measurement of T1 relaxation times at 3.0T: Implications for clinical MRA* (p. 1391). Proceedings of the International Society for Magnetic Resonance in Medicine.

Liu, H., Dai, Z., So, D. R., & Le, Q. V. (2021). Pay attention to MLPSs. *Advances in Neural Information Processing Systems*, *34*, 9204–9215.

Liu, J., Wang, Y., Katscher, U., & He, B. (2017). Electrical properties tomography based on B1 maps in MRI: Principles, applications, and challenges. *IEEE Transactions on Biomedical Engineering*, *64*(11), 2515–2530.

Liu, J., Xiaotong, Z., Schmitter, S., Van de Moortele, P.-F., & He, B. (2015). Gradient-based electrical properties tomography (g EPT): A robust

method for mapping electrical properties of biological tissues in vivo using magnetic resonance imaging. *Magnetic Resonance in Medicine*, *74*(3), 634–646.

Lu, H., Nagae-Poetscher, L. M., Golay, X., Lin, D., Pomper, M., & van Zijl, P. C. M. (2005). Routine clinical brain MRI sequences for use at 3.0 Tesla. *Journal of Magnetic Resonance Imaging*, *22*(1), 13–22.

Mandija, S., Meliadò, E. F., Huttinga, N. R. F., Luijten, P. R., & van den Berg, C. A. T. (2019). Opening a new window on MR-based electrical properties tomography with deep learning. *Scientific Reports*, *9*(1), 1–9.

Mandija, S., Petrov, P. I., Vink, J. J. T., Neggers, S. F. W., & van den Berg, C. A. T. (2021). Brain tissue conductivity measurements with MR-electrical properties tomography: An in vivo study. *Brain Topography*, *34*(1), 56–63.

Mandija, S., Sbrizzi, A., Katscher, U., Luijten, P. R., & van den Berg, C. A. T. (2018). Error analysis of Helmholtz-based MR-electrical properties tomography. *Magnetic Resonance in Medicine*, *80*(1), 90–100.

Meerbothe, T. G., Florczak, S., Stijnman, P. R. S., van den Berg, C. A. T., Levato, R., & Mandija, S. (2022). *A semi-realistic and reusable 3D printed brain phantom for MR-based electrical properties tomography* (p. 2921). Proceedings of the international society for magnetic resonance in medicine.

Michel, E., Hernandez, D., Cho, M. H., & Lee, S. Y. (2014). Denoising of B1+ field maps for noise-robust image reconstruction in electrical properties tomography. *Medical Physics*, *41*(10), 102304.

Mori, N., Tsuchiya, K., Sheth, D., Mugikura, S., Takase, K., Katscher, U., & Abe, H. (2019). Diagnostic value of electric properties tomography (EPT) for differentiating benign from malignant breast lesions: Comparison with standard dynamic contrast-enhanced MRI. *European Radiology*, *29*(4), 1778–1786.

Murphy, M. C., Manduca, A., Trzasko, J. D., Glaser, K. J., Huston, J., III, & Ehman, R. L. (2018). Artificial neural networks for stiffness estimation in magnetic resonance elastography. *Magnetic Resonance in Medicine*, *80*(1), 351–360.

Paszke, A., Gross, S., Massa, F., Lerer, A., Bradbury, J., Chanan, G., Killeen, T., Lin, Z., Gimelshein, N., Antiga, L., Desmaison, A., Kopf, A., Yang, E., DeVito, Z., Raison, M., Tejani, A., Chilamkurthy, S., Steiner, B., Fang, L., … Chintala, S. (2019). PyTorch: An imperative style, high-performance deep learning library. *Advances in Neural Information Processing Systems*, *32*, 8024–8035.

Raissi, M., Perdikaris, P., & Karniadakis, G. E. (2019). Physics-informed neural networks: A deep learning framework for solving forward and inverse problems involving nonlinear partial differential equations. *Journal of Computational Physics*, *378*, 686–707.

Ronneberger, O., Fischer, P., & Brox, T. (2015). U-Net: Convolutional networks for biomedical image segmentation. *Proceedings of the International Conference on Medical Image Computing and Computer-Assisted Intervention*, *18*, 234–241.

Roy, A. G., Conjeti, S., Navab, N., Wachinger, C., & Alzheimer's Disease Neuroimaging Initiative. (2019). Bayesian QuickNAT: Model uncertainty in deep whole-brain segmentation for structure-wise quality control. *NeuroImage*, *195*, 11–22.

Sabati, A., & Maudsley, A. A. (2013). Fast and high-resolution quantitative mapping of tissue water content with full brain coverage for clinically-driven studies. *Magnetic Resonance Imaging*, *31*(10), 1752–1759.

Schmidt, R., & Webb, A. (2016). A new approach for electrical properties estimation using a global integral equation and improvements using high permittivity materials. *Journal of Magnetic Resonance*, *262*, 8–14.

Seo, J. K., Kim, M. O., Lee, J., Choi, N., Woo, E. J., Kim, H. J., Kwon, O. I., & Kim, D. H. (2011). Error analysis of nonconstant admittivity for MR-based electric property imaging. *IEEE Transactions on Medical Imaging*, *31*(2), 430–437.

Serrallés, J. E. C., Giannakopoulos, I. I., Zhang, B., Lanniello, C., Cloos, M. A., Polimeridis, A. G., White, J. K., Sodickson, D. K., & Lattanzi, R. (2019). Noninvasive estimation of electrical properties from magnetic resonance measurements via global Maxwell tomography and match regularization. *IEEE Transactions on Biomedical Engineering*, *67*(1), 3–15.

Shattuck, D. W., & Leahy, R. M. (2002). BrainSuite: An automated cortical surface identification tool. *Medical Image Analysis*, *6*(2), 129–142.

Shin, J., Kim, M. J., Lee, J., Nam, Y., Kim, M. O., Choi, N., Kim, S., & Kim, D. H. (2015). Initial study on in vivo conductivity mapping of breast cancer using MRI. *Journal of Magnetic Resonance Imaging*, *42*(2), 371–378.

Shin, J., Kim, J. H., & Kim, D. H. (2019). Redesign of the Laplacian kernel for improvements in conductivity imaging using MRI. *Magnetic Resonance in Medicine*, *81*(3), 2167–2175.

Smith, S. M., Jenkinson, M., Woolrich, M. W., Beckmann, C. F., Behrens, T. E. J., Johansen-Berg, H., Bannister, P. R., Luca, M. D., Drobnjak, I., Flitney, D. E., Niazy, R. K., Saunders, J., Vickers, J., Zhang, Y., De Stefano, N., Brady, J. M., & Matthews, P. M. (2004). Advances in functional and structural MR image analysis and implementation as FSL. *NeuroImage*, *23*(1), S208–S219.

Spijkerman, J. M., Petersen, E. T., Hendrikse, J., Luijten, P., & Zwanenburg, J. J. M. (2018). T2 mapping of cerebrospinal fluid: 3T versus 7T. *Magnetic Resonance Materials in Physics, Biology and Medicine*, *31*(3), 415–424.

Stanisz, G. J., Odrobina, E. E., Pun, J., Escaravage, M., Gramham, S. J., Bronskill, M. J., & Henkelman, R. M. (2015). T1, T2 relaxation and magnetization transfer in tissue at 3T. *Magnetic Resonance in Medicine*, *54*(3), 507–512.

Suh, J., Kim, J. H., Kim, S. Y., Cho, N., Kim, D. H., Kim, R., Kim, E. S., Jang, M. J., Ha, S. M., Lee, S. H., Chang, J. M., & Moon, W. K. (2021). Noncontrast-enhanced MR-based conductivity imaging for breast cancer detection and lesion differentiation. *Journal of Magnetic Resonance Imaging*, *54*(2), 631–645.

Tanno, R., Worrall, D. E., Kaden, E., Ghosh, A., Grussu, F., Bizzi, A., Sotiropoulos, S. N., Criminisi, A., & Alexander, D. C. (2021). Uncertainty modelling in deep learning for safer neuroimage enhancement: Demonstration in diffusion MRI. *NeuroImage*, *225*, 117366.

Tha, K. K., Katscher, U., Yamaguchi, S., Stehning, C., Terasaka, S., Fujima, N., Kudo, K., Kazumata, K., Yamamoto, T., Van Cauteren, M., & Shirato, H. (2018). Noninvasive electrical conductivity measurement by MRI: A test of its validity and the electrical conductivity characteristics of glioma. *European Radiology*, *28*(1), 348–355.

Tha, K. K., Stehning, C., Suzuki, Y., Katscher, U., Keupp, J., Kazumata, K., Terasaka, S., Van Cauteren, M., Kudo, K., & Shirato, H. (2014). Noninvasive evaluation of electrical conductivity of the normal brain and brain tumors. *Proceedings of the International Society for Magnetic Resonance in Medicine*, *1885*.

Ulyanov, D., Vedaldi, A., & Lempitsky, V. (2020). Deep image prior. *International Journal of Computer Vision*, *128*(7), 1867–1888.

van den Bergen, B., Stolk, C. C., van den Berg, J. B., Lagendijk, J. J. W., & Van den Berg, C. A. T. (2009). Ultra fast electromagnetic field computations for RF multi-transmit techniques in high field MRI. *Physics in Medicine & Biology*, *54*(5), 1253–1264.

van Lier, A. L. H. M. W., Brunner, D. O., Pruessmann, K. P., Klomp, D. W. J., Luijten, P. R., Lagendijk, J. J. W., & van den Berg, C. A. T. (2012). B1+ phase mapping at 7T and its application for in vivo electrical conductivity mapping. *Magnetic Resonance in Medicine*, *67*(2), 552–561.

Voigt, T., Homann, H., Katscher, U., & Doessel, O. (2012). Patient-individual local SAR determination: In vivo measurements and numerical validation. *Magnetic Resonance in Medicine*, *68*(4), 1117–1126.

Voigt, T., Katscher, U., & Doessel, O. (2011). Quantitative conductivity and permittivity imaging of the human brain using electric properties tomography. *Magnetic Resonance in Medicine*, *66*(2), 456–466.

Yu, X., Serrallés, J. E. C., Giannakopoulos, I. I., Liu, Z., Daniel, L., Lattanzi, R., & Zhange, Z. (2023). PIFON-EPT: MR-based electrical property tomography using physics-informed Fourier networks. *arXiv Preprint* arXiv:2302.11883.

Zhang, X., Schmitter, S., Van de Moortele, P. F., Liu, J., & He, B. (2013). From complex B1 mapping to local SAR estimation for human brain MR imaging using multi-channel transceiver coil at 7T. *IEEE Transactions on Medical Imaging*, *32*(6), 1058–1067.

SUPPORTING INFORMATION

Additional supporting information can be found online in the Supporting Information section at the end of this article.

How to cite this article: Jung, K.-J., Mandija, S., Cui, C., Kim, J.-H., Al-masni, M. A., Meerbothe, T. G., Park, M., van den Berg, C. A. T., & Kim, D.-H. (2023). Data-driven electrical conductivity brain imaging using 3 T MRI. *Human Brain Mapping*, *44*(15), 4986–5001. https://doi.org/10.1002/hbm.26421